TU Delft

Delft University of Technology

Document Version
Final published version

Licence
CC BY

Citation (APA)
Kunkels, L. B., Yang, J., Klimopoulou, M., Yarali, E., Li, L. J., Leeflang, M. A., Tas, R. P., Fratila-Apachitei, L. E., Zadpoor, A. A., & Mirzaali, M. J. (2026). Multi-objective design and validation of a bioinspired tri-zonal scaffold for tendon-bone interfaces. *Materials and Design*, *272*, Article 117305. https://doi.org/10.1016/j.matdes.2026.117305

Important note
To cite this publication, please use the final published version (if applicable).
Please check the document version above.

Copyright
In case the licence states “Dutch Copyright Act (Article 25fa)”, this publication was made available Green Open Access via the TU Delft Institutional Repository pursuant to Dutch Copyright Act (Article 25fa, the Taverne amendment). This provision does not affect copyright ownership.
Unless copyright is transferred by contract or statute, it remains with the copyright holder.

Sharing and reuse
Other than for strictly personal use, it is not permitted to download, forward or distribute the text or part of it, without the consent of the author(s) and/or copyright holder(s), unless the work is under an open content license such as Creative Commons.

Takedown policy
Please contact us and provide details if you believe this document breaches copyrights.
We will remove access to the work immediately and investigate your claim.

This work is downloaded from Delft University of Technology.

Materials & Design 272 (2026) 117305

Contents lists available at ScienceDirect

Materials & Design

journal homepage: www.elsevier.com/locate/matdes

Multi-objective design and validation of a bioinspired tri-zonal scaffold for tendon-bone interfaces

L.B. Kunkels [a,*], J. Yang [a,b], M. Klimopoulou [a], E. Yarali [a], J. Li [a], M.A. Leeflang [a], R.P. Tas [a], L.E. Fratila-Apachitei [a], A.A. Zadpoor [a], M.J. Mirzaali [a,*]

[a] Department of Biomechanical Engineering, Faculty of Mechanical Engineering, Delft University of Technology (TU Delft), Mekelweg 2, 2628 CD Delft, the Netherlands
[b] College of Mechanical Engineering and Automation, Huaqiao University, Xiamen 361021, China

ARTICLE INFO

Keywords:
Tendon-bone interface
Multi-objective design
Additive manufacturing
Stiffness gradients
Scaffold architecture

ABSTRACT

The tendon-bone interface exhibits a complex gradient in mechanical and morphological properties, enabling robust load transfer between soft and hard tissues. Replicating this functionality in engineered scaffolds remains challenging. Here, we present a computational-experimental framework for developing tri-zonal scaffolds with spatially varying stiffness and zone-specific architectures for tendon-bone interface applications. A hybrid lattice combining strut-based and surface-based geometries was used to generate tendon-like, transitional, and bone-like zones. Homogenization-based modeling and 3D finite element simulations were used to screen 36 feasible design configurations. Two representative designs were fabricated *via* fused deposition modeling and integrated with an alginate-gelatin hydrogel. Micro-computed tomography was used to assess manufacturing fidelity, and identify architecture-dependent geometric deviations, while mechanical testing characterized the response of the fabricated scaffolds and hydrogel-integrated constructs. Design A exhibited a 72-93% higher maximum tensile force than Design B, with failure observed predominantly within the hydrogel adjacent to the scaffold-hydrogel interface. Preliminary *in vitro* observations with MC3T3-E1 preosteoblasts showed qualitative differences in cell morphology and spatial organization between scaffold architectures and zones. These findings demonstrate the use of a multi-objective design framework for integrating zone-specific mechanical and morphological requirements and provide a basis for further development of engineered soft-hard tissue interfaces.

1. Introduction

Over millions of years of evolution, nature has developed complex soft-hard interfaces that exhibit remarkable strength, resilience, and the capacity to seamlessly integrate materials with vastly different mechanical properties [1]. These interfaces enable efficient load transfer and minimize stress concentrations, thereby preventing failure under static (*e.g.*, body weight) or dynamic (*e.g.*, cyclic) loading scenarios [2]. A recognized example is the tendon-bone interface, or enthesis (Fig. 1a), where the soft tendon (elastic modulus = 0.2–0.6 GPa [3]) connects directly to the much stiffer bone (elastic modulus = 3–30 GPa [4,5]) through a narrow transitional region. This zone, typically only spanning a few millimeters, is characterized by complex morphological interdigitations, graded material compositions along the interface, and anisotropic structural orientations, accompanied by distinct distributions of tissue-specific cell types [6–9].

Engineering constructs that replicate this biological complexity remains a persistent challenge. The extreme mechanical mismatch between soft and hard tissues often leads to failure at the interface, particularly when fabricated using conventional (subtractive) methods [10]. Such methods typically produce abrupt material transitions that introduce stress concentrations, delamination, and compromised load-bearing capacity [11–14]. Alternative strategies, such as adhesive bonding, composite layering, or mechanical interlocks, offer limited improvements, often at the expense of mechanical integrity, biocompatibility, or geometric fidelity [15,16].

In response, several studies have increasingly focused on "multiphasic scaffold architectures" that aim to replicate the structural and mechanical gradients found in native entheses. These designs typically incorporate multiple zones with distinct material properties and geometries to bridge the soft-hard transition [2,16]. While these approaches have shown promise in enhancing mechanical performance and supporting cellular integration, they still face critical limitations. In particular, many of these designs often fail to capture the full range of

* Corresponding authors.
E-mail addresses: L.B.Kunkels@tudelft.nl (L.B. Kunkels), M.J.Mirzaali@tudelft.nl (M.J. Mirzaali).

https://doi.org/10.1016/j.matdes.2026.117305
Received 7 August 2026; Received in revised form 6 October 2026; Accepted 19 October 2026
Available online 24 October 2026
0264-1275/© 2026 The Author(s). Published by Elsevier Ltd. This is an open access article under the CC BY license (http://creativecommons.org/licenses/by/4.0/).

mechanical and morphological properties required for seamless integration between mechanically dissimilar soft and hard tissues, and few explicitly address the multi-objective biomimetic design principles inherent to such interfaces. Examples include gradient bipolar nanofiber scaffolds [17], biphasic silk fibroin scaffolds [18], and triphasic scaffolds combining fused deposition modeling (FDM) and electrospinning [19], each of which mimics selected aspects of the enthesis but falls short in others.

Recent advances in architected scaffolds have expanded the range of microstructures available for bone tissue regeneration. Triply periodic minimal surface (TPMS) architectures are particularly attractive because their continuous and interconnected pore networks enable

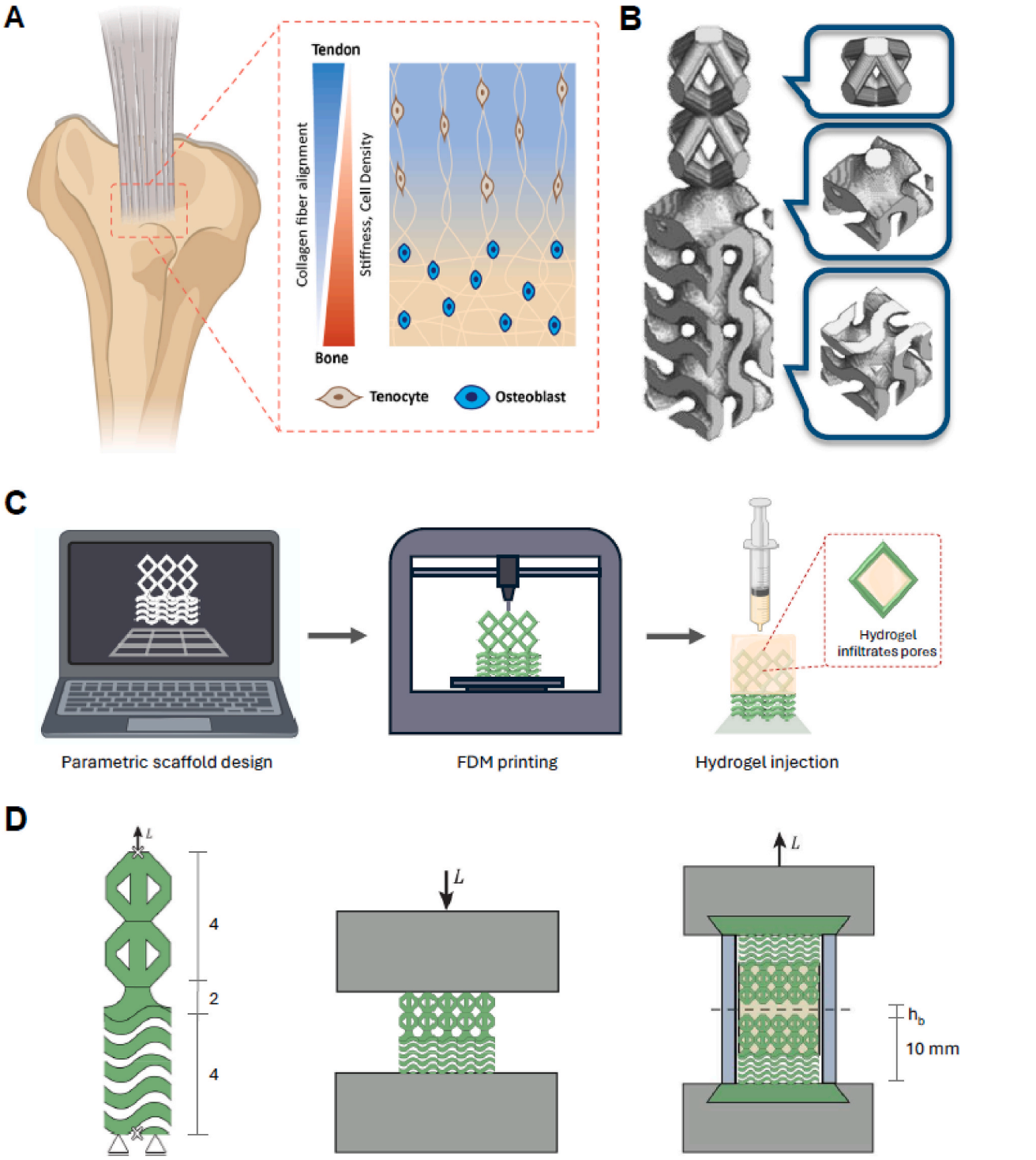


Fig. 1. **a.** An anatomical schematic drawing of the tendon-bone interface (enthesis), highlighting the natural compositional and mechanical gradient. **b.** Design of tri-zonal scaffold, consisting of three interconnected zones: a bone-like (hard) gyroid structure, a transition region, and a tendon-like (soft) strut-based geometry. **c.** A schematic overview of the scaffold fabrication process: parametric design (left), FDM 3D printing (middle), and hydrogel injection into the tendon-like region (right). **d.** An overview of experimental and computational setups: finite element model (left), compression testing configuration (middle), and tensile testing configuration (right). Scaffold-zone dimensions are given in mm. h_0 denotes the inter-scaffold separation, corresponding to the hydrogel-layer thickness. Loading direction (L) is indicated by arrows.

simultaneous control over porosity, permeability, and mechanical properties. For example, gradient TPMS scaffolds inspired by the Haversian system have been shown to improve fluid transport and stress transfer while promoting bone ingrowth [20]. Trabecular-like architectures provide a complementary strategy by generating irregular, interconnected pore networks that more closely resemble the heterogeneous organization of cancellous bone. Recent work further demonstrated that architectural parameters such as porosity can regulate the local fluid shear stress experienced by cells, thereby influencing osteogenic differentiation and bone regeneration [21]. These studies highlight the importance of scaffold architecture not only for reproducing bone-like mechanical and morphological properties but also for regulating the local biological microenvironment. However, these approaches primarily address the requirements of bone regeneration. Engineering the tendon-bone enthesis additionally requires a coordinated transition from a compliant and highly anisotropic tendon-like region to a stiffer and relatively isotropic bone-like region. This motivates the use of distinct, zone-specific architectures within an integrated scaffold design.

Despite recent progress, three limitations remain common in tendon-bone interface scaffold design. First, many multiphasic approaches primarily introduce compositional gradients without simultaneously differentiating the underlying lattice topology required to reproduce the highly anisotropic tendon region and relatively isotropic bone region [7]. Second, design selection is often empirical rather than based on quantitative multi-objective optimization of conflicting mechanical and morphological requirements [22]. Third, transition regions are frequently simplified, limiting control over the mechanical mismatch between adjacent zones [7,18]. These limitations motivate the use of zone-specific architectures combined within a systematic optimization framework.

The challenge arises from the conflicting design requirements across different scaffold zones dedicated to soft or hard tissues [10]. For example, tendon-like regions require low stiffness, high anisotropy, and larger pore sizes (~400–700 μm) to support fibroblast and tenocyte infiltration [23], whereas bone-like regions demand high stiffness, relatively isotropic behavior, and smaller pores (~200–400 μm) to enable osseointegration [24–26]. These parameters are mutually interdependent. In this regard, for example, increasing stiffness typically results in reduced porosity. Enhancing anisotropy in one region may compromise mechanical behavior at the interface, as it must accommodate the isotropic behavior on the other side of the scaffold. Optimizing the performance of one region often comes at the expense of the other. Moreover, the transitional zone must accommodate a smooth mechanical and morphological gradient across these competing requirements, further complicating the scaffold design space for such interfaces.

Addressing this issue requires a systematic and flexible design platform that can resolve these trade-offs. One promising strategy involves the use of hybrid lattice architectures, such as combining strut-based designs for the tendon region with surface-based geometries for the bone region [27]. This approach enables spatially controlled tuning of mechanical and morphological properties, facilitating more physiologically relevant scaffold designs.

In this study, we therefore present a computational and experimental framework to tackle the multi-objective design problem for tendon-bone interface scaffolds. Using validated homogenization-based parametric simulations, we explore the mechanical and morphological design space of a tri-zonal (three-zone) scaffold combining strut-based geometries for the tendon zone and surface-based geometries for the bone zone, connected through a graded transition zone (Fig. 1b), aiming to identify hybrid geometries that satisfy the distinct and sometimes conflicting requirements of each region. The resulting designs were fabricated using additive manufacturing (AM) and subsequently characterized morphologically and mechanically.

To further evaluate the biological relevance of our proposed designs, preliminary *in vitro* studies using MC3T3-E1 preosteoblasts were conducted to assess their cell morphology and spatial distribution on the different scaffold designs and across different zones.

This integrated design and validation framework provides a foundation for the development of next-generation (interface) scaffolds that emulate the functional and structural complexity of native soft-hard tissue interfaces. Such strategies hold promises for advancing applications in musculoskeletal tissue engineering, regenerative medicine, and multi-phasic implant systems.

2. Results and discussion

2.1. Homogenization-based exploration of the tri-zonal scaffold design space

To address the mechanical and morphological design challenges of the tendon-bone interface, we conducted a homogenization-based parametric study to explore the mechanical and morphological property space of a tri-zonal scaffold architecture. The scaffold design was composed of three zones: 1. a strut-based, low-density lattice for the tendon-like zone, 2. a surface-based, high-density gyroid TPMS structure for the bone-like zone, and 3. a transitional zone composed of a continuous TPMS Schwarz primitive surface to bridge the two extremes (Fig. 1b). Fig. 1c, d illustrates the fabrication process and experimental setup.

The scaffold design was parameterized using two inputs: tendon-zone density (ρ_t) and bone-zone density (ρ_b), each ranging between 5% and 60% (Fig. 2a, c). Configurations containing a density of 0.05 in either zone were excluded because the corresponding voxelized architectures exhibited structural discontinuities, resulting in 36 feasible configurations for subsequent homogenization and optimization. For each design, seven key metrics were evaluated through numerical homogenization: four mechanical parameters (*i.e.*, Zener ratio, Poisson's ratio, normalized elastic modulus, and stiffness ratio) and three morphological parameters (*i.e.*, pore size, solid volume fraction, and surface area) (Fig. 2b–c).

We first report the global range of values for all seven criteria across the entire design space, and then provide an in-depth, zone-specific analysis of the relationships between input parameters and scaffold behavior. Mechanical and morphological parameters are treated in separate sub-sections to clarify their distinct roles in the design process.

2.2. Morphological characteristics across the scaffold design space

Pore size (d_p) was inversely related to density in both tendon- and bone-like regions. In the tendon region, pore diameters ranged between 750 μm (ρ_t = 5%) and 410 μm (ρ_t = 60%). In the bone region, pores ranged from 380 μm (ρ_b = 5%) to 230 μm (ρ_b = 60%). In the transitional zone, pore size ranged from 480 μm at minimum densities to 310 μm at maximum densities. These trends indicate direct tunability of porosity through the input parameters, which is critical for matching cell-specific infiltration thresholds.

Solid volume fraction (*SVF*) increased linearly with ρ_t and ρ_b in tendon and bone regions, respectively. In the tendon zone, *SVF* ranged between 0.038 (ρ_t = 5%) and 0.61 (ρ_t = 60%). In the bone zone, values spanned 0.05–0.60. In the transitional zone, *SVF* varied from 0.07 to 0.63, with a stronger dependence on ρ_b. For example, at ρ_t = 60% and ρ_b = 5%, *SVF* was 0.28, while at ρ_t = 5% and ρ_b = 60%, *SVF* increased to 0.47. This indicates the bone-side architecture has a dominant effect on material distribution across the transition.

Surface area (*A*) increased in a density-dependent manner in all regions. In the tendon-like zone, values ranged from 5.75 to 18.2 mm^2, and in the bone-like zone from 17.86 to 31.43 mm^2. In the transitional region, the surface area ranged from 19.32 to 25.51 mm^2, increasing symmetrically with both inputs. Unlike *SVF*, surface area was equally influenced by both ρ_t and ρ_b, suggesting balanced geometric

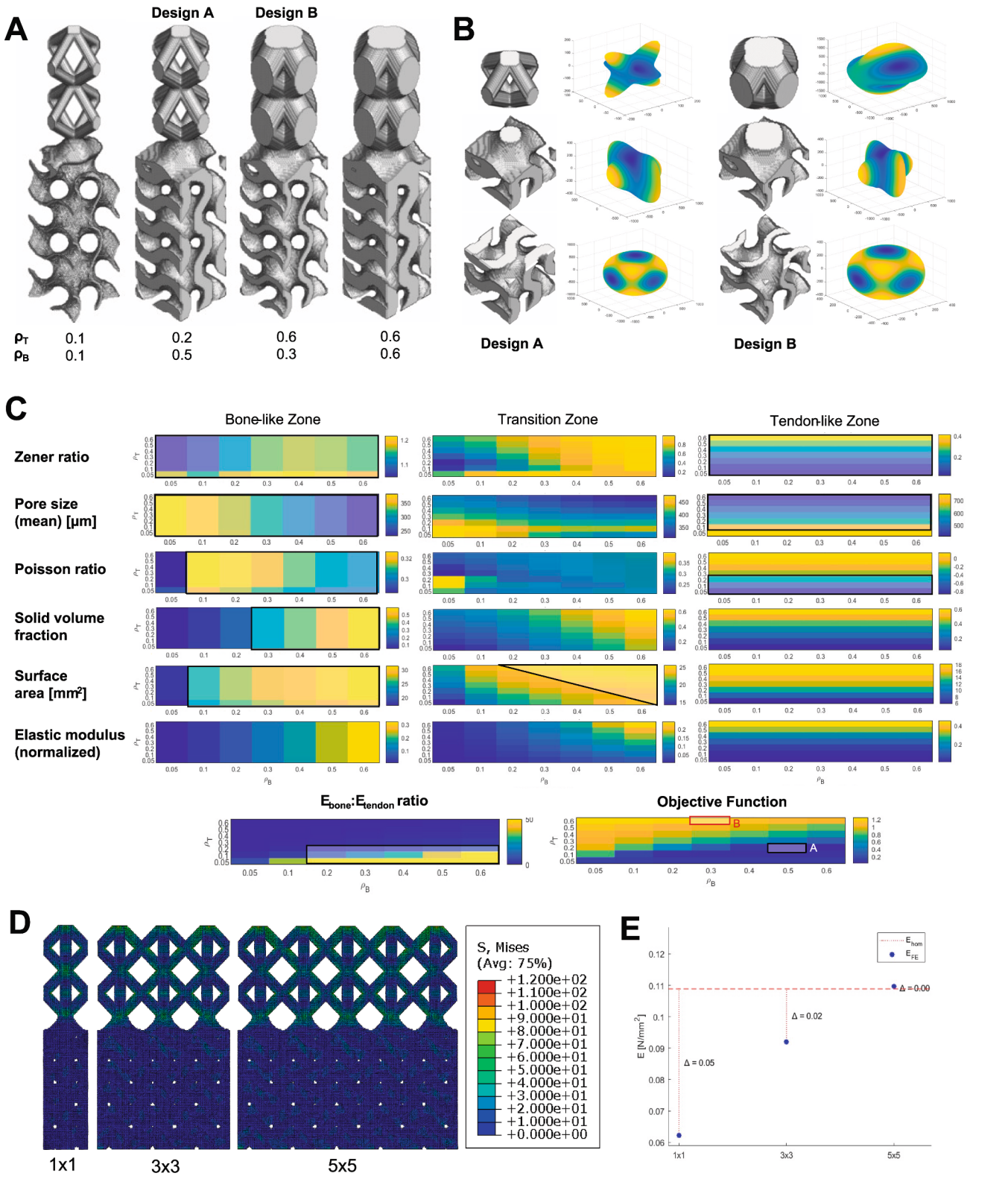


Fig. 2. **A.** Parametric design output showing how variations in input parameters (bone density, ρ_b and tendon density, ρ_t) affect the geometry of each scaffold region. **b.** Stiffness maps for each zone of Design A and Design B, illustrating spatial anisotropy and directional mechanical response. **c.** Heatmaps from the homogenization study showing the influence of bone-zone density (ρ_b) and tendon-zone density (ρ_t) on the evaluated mechanical and morphological parameters. The horizontal and vertical axes represent ρ_b and ρ_t, respectively. Pore size is reported in μm and surface area in mm^2; all other quantities are dimensionless. Black borders indicate configurations satisfying all predefined constraints, while the red border indicates the selected suboptimal Design B. **d.** Finite-element results showing von Mises stress distributions; stress values are reported in MPa. **e.** Comparison of the effective elastic modulus across varying numbers of unit cells, demonstrating convergence toward the homogenization prediction (red dashed line). (For interpretation of the references to colour in this figure legend, the reader is referred to the web version of this article.)

contributions from both scaffold types. Higher surface area is expected to support improved protein adsorption and cellular attachment at the soft-hard interface [28].

2.3. Mechanical behavior and anisotropy across the scaffold design space

The scaffolds exhibited tunable Poisson's ratio (ν) across the design space. The tendon region showed auxetic behavior ($\nu < 0$) at low densities (*e.g.*, $\nu = -0.88$ at $\rho_t = 5\%$) and transitioned to conventional values ($\nu > 0$) at higher densities ($\nu = 0.14$ at $\rho_t = 60\%$). In the bone region, Poisson's ratio peaked at 0.33 ($\rho_b = 10\%$) and declined slightly to 0.30 at $\rho_b = 60\%$. In the transitional zone, the values ranged from 0.25 to 0.30, with peak values observed at the edges of the design space. The auxetic response at low tendon-zone density is attributed to the greater rotational and bending freedom of the slender strut network, which is consistent with lateral expansion under axial loading. As the tendon-zone density increases, these deformation modes become more constrained, and the Poisson's ratio shifts toward conventional positive values. This demonstrates that scaffold auxeticity can be controlled through local geometry, relevant for energy dissipation and auxetic behavior of the tendon region.

The Zener ratio (z), which is a metric for anisotropy, showed highly region-specific trends. In the tendon zone, low-density structures were highly anisotropic (*e.g.*, $z = 0.014$ at $\rho_t = 5\%$), tending toward an isotropic morphology as ρ_t increased ($z = 0.42$ at $\rho_t = 60\%$). In contrast, the bone zone became more anisotropic for higher density values (although still more isotropic than the tendon zone), reaching a peak of $z = 1.17$ at $\rho_b = 40\%$, followed by a slight decline. The transitional zone was sensitive to both inputs, with z peaking at 0.99 when ρ_t and ρ_b were both high. These results demonstrate the ability to tune anisotropy across regions, which is critical for replicating the direction-dependent behavior of native tissue.

Normalized elastic modulus ($E_{norm} = E/E_{PLA}$, where $E_{PLA} = 3071$ MPa is the Young's modulus of PLA) showed distinct input-dependent trends. In the tendon region, E_{norm} increased from 0.00075 to 0.46 as ρ_t increased. In the bone region, the values ranged from 0.0062 to 0.32 for increasing ρ_b values. The higher effective modulus of the bone-like Gyroid region arises from its continuous sheet-based load paths and the increased solid fraction at higher density, which together provide a more distributed load-bearing network within the unit cell. In the transitional zone, modulus values spanned 0.00050–0.25, with a notably stronger dependence on ρ_b than ρ_t. For instance, when $\rho_t = 5\%$ and $\rho_b = 60\%$, E_{norm} reached 0.085, as compared to 0.0075 for the reversed condition. This reflects the dominant structural stiffness contribution of the bone-like architecture.

Bone-to-tendon modulus ratio ($E_b : E_t$). Derived from the normalized elastic moduli, the modulus ratio spanned a wide range, from 0.060 to 51.97, depending on ρ_t and ρ_b combinations. The highest ratios were observed at low ρ_t and high ρ_b, illustrating the design's ability to replicate the substantial stiffness gradient found at the natural enthesis. These trends further highlight the importance of coordinated density tuning across scaffold zones.

These results demonstrate that the hybrid design space can span the full spectrum of required scaffold properties across tendon, transition, and bone zones. The trade-offs between mechanical and morphological parameters highlight the need for a multi-objective design strategy, where optimizing one parameter (*e.g.*, stiffness) may have adverse impacts on another (*e.g.*, porosity or anisotropy). In the next section, candidate scaffold designs are selected based on their ability to meet these competing requirements.

2.4. Design selection based on multi-objective criteria

To identify scaffold configurations capable of replicating the functional complexity of the tendon-bone interface, we established six quantitative design criteria (marked where applicable in Fig. 2c) based on key mechanical and morphological parameters. These thresholds were derived from literature reports on native tendon and bone tissue requirements, considering both biological performance and structural integrity:

1. Elastic modulus ratio ($E_b : E_t$): Target range >9 to reflect tendon-bone contrast [3,4].
2. Poisson's ratio: Auxetic or near-zero behavior for tendon (−1.44 to −0.39), conventional behavior for bone (0.3–0.35) [29,30].
3. Zener ratio (z): High anisotropy in tendon ($|z-1| \gg 0$), near-isotropy in bone ($z \approx 1$) [9,31,32].
4. Pore size: 400–700 μm for tendon, 200–400 μm for bone [23,25,26].
5. Solid volume fraction (*SVF*): Sufficient for load bearing but porous enough for infiltration with a target of 0.26–0.75 for bone [33].
6. Surface area: Increased surface area promotes cell attachment and tissue integration, with a large surface area-to-volume ratio (>30 cm^{-1}) being preferred [34].

To identify scaffold configurations capable of replicating the functional complexity of the tendon-bone interface, we established six quantitative design criteria based on key mechanical and morphological parameters. These criteria included: (1) elastic-modulus ratio, (2) Poisson's ratio, (3) Zener ratio, (4) pore size, (5) solid volume fraction, and (6) surface-area-to-volume ratio. Because several properties were evaluated independently in the tendon-like and bone-like zones, and surface area was evaluated in all three zones, these six categories were represented by 11 individual normalized penalty terms in the objective function. Architectural transition across the tendon-like, transitional, and bone-like regions was addressed separately through the Schwarz-P transitional geometry [35], and was not included as an independent numerical penalty term.

Among the 36 candidate scaffold designs evaluated in the parametric study, two representative configurations were selected by minimizing the objective function OF(ρ_b, ρ_t) (Eq. (6)): (*i*) Optimal configuration (Design A): Defined by $\rho_t = 20\%$ (tendon side) and $\rho_b = 50\%$ (bone side). This design satisfied all six quantitative criteria mentioned above and exhibited continuous architectural integration across the three zones. It provided high anisotropy and auxeticity in the tendon zone, near-isotropic and stiff behavior in the bone zone, and a smooth transition with intermediate pore size and stiffness. Surface area and *SVF* were also within biologically relevant ranges across all the zones. (*ii*) Suboptimal configuration (Design B): defined by $\rho_t = 60\%$ and $\rho_b = 30\%$. This design met only four out of the six quantitative criteria. While it remained 3D printable and structurally continuous, it exhibited suboptimal stiffness gradient, lacked sufficient anisotropy in the tendon region, and failed to meet the pore size requirements for either cell type. Design B was selected as a deliberately suboptimal, yet printable, reference configuration to illustrate the consequences of deviating from the predefined mechanical and morphological design targets.

An a posteriori Pareto analysis of the 36 computationally feasible configurations identified 10 non-dominated designs (Fig. S2 and Table S2 of the supplementary document). Design A ($\rho_b = 0.5$, $\rho_t = 0.2$) belonged to the Pareto-optimal set, whereas Design B ($\rho_b = 0.3$, $\rho_t = 0.6$) was dominated by seven alternative configurations. The configuration (ρ_b, ρ_t) = (0.6, 0.2) was also Pareto-optimal and had the same total objective-function value as Design A. Design A was retained for fabrication because its lower bone-zone density provided equivalent performance according to the scalar objective function while reducing the likelihood of pore occlusion associated with the higher-density alternative. The Pareto analysis therefore supports Design A as a non-dominated solution within the explored design space rather than establishing it as a unique optimum.

Criterion-weight sensitivity analysis showed that Design A remained rank 1 under all tested weighting scenarios and was consistently tied with the (ρ_b, ρ_t) = (0.6, 0.2) configuration (Table S3 of the

supplementary document). This result indicates that the ranking of Design A was robust to the tested moderate variations in the relative weighting of the predefined criteria.

2.5. Stiffness distribution and zone-specific mechanical behavior

To further compare the structural responses of the two selected scaffold designs, we generated spatial stiffness distribution maps based on the homogenization results. These maps revealed zone-specific stiffness patterns that correspond to the underlying lattice geometry and input densities (Fig. 2b).

In this regard, in the bone-like region, both Designs A and B exhibited relatively isotropic stiffness patterns, with peak effective stiffness values around 500 MPa for Design A and 200 MPa for Design B (Fig. 2b, bottom row). These values reflect the higher density and surface-based geometry of the bone zone in Design A, supporting its suitability for load-bearing applications. In the transitional region, both designs showed anisotropic stiffness maps with characteristic plus-shaped patterns (Fig. 2b, middle row). However, the orientation and intensity of these patterns differed, suggesting differences in how mechanical forces would be redistributed across the interface under load. This zone is crucial for reducing stress concentrations between mismatched materials and geometries. In the tendon-like region, the distinction between the two designs was most pronounced. Design A produced a star-shaped anisotropic stiffness pattern, consistent with energy-dissipative behavior typical of tendon tissue (Fig. 2b, top row). In contrast, Design B generated a more rounded, isotropic stiffness profile, deviating from the native tendon characteristics and potentially leading to less favorable mechanical behavior under tensile loading.

Across the full scaffold, both designs exhibited higher stiffness values, concentrated along the *x*- and *y*-axes; however, only Design A maintained zone-specific mechanical profiles aligned with functional tissue requirements (Fig. 1a). This highlights the importance of coordinated density and geometry control in achieving spatially programmed mechanical behavior.

2.6. Finite element modeling of tri-zonal scaffold behavior

To complement the homogenization-based parametric analysis and assess the mechanical behavior of the full scaffold architecture (for both Design A and B) under realistic loading conditions, finite element (FE) simulations were performed using Abaqus. The simulations modeled the response of the complete tri-zonal scaffold, including tendon-like, transitional, and bone-like regions, under both tensile and compressive loading (Fig. 1d illustrates these loading configurations). These simulations provided a mesoscale view of how local lattice geometries influence global load transfer, deformation, and stress distribution across the multi-geometry interfaces.

Stress contour maps (Fig. 2d) under uniaxial loading revealed that peak stress concentrations were localized in the tendon-like zone, particularly around the strut junctions in the strut-based lattice. These areas represent potential mechanical weak points under high tensile strain. In contrast, the transitional region effectively redistributed the load and exhibited a smooth stress gradient between two extreme geometries (*i.e.*, strut-based and surface-based lattice designs). The absence of abrupt stress discontinuities at the tendon-bone junction indicates that the transitional region exhibited intermediate elastic stress levels between the tendon-like and bone-like architectures. These results support the functional role of the transitional zone in mitigating stress concentrations and promoting seamless load transfer across the interface. The transition cells also transfer the location of the failure towards the tendon-like regions, similar to what occurs in the native tissue failure [36,37].

To assess whether homogenization-based elastic moduli are representative for scaffolds with a limited number of unit cells, a convergence analysis was conducted by simulating scaffolds composed of different numbers of repeated unit cells in the lateral (width-wise) direction. Scaffold models with 1, 3, and 5 repeated unit cells were subjected to tensile loading, and the resulting global stiffness values were compared to those predicted *via* voxel-based homogenization (Fig. 2e). For scaffolds with only one- or three-unit cells, the predicted elastic moduli were consistently lower than those obtained from homogenization. This deviation was attributed to edge effects and insufficient structural periodicity, which affect the load path and strain distribution in small-scale models. When the scaffold contained five repeated unit cells, the simulated modulus converged closely to the homogenized prediction. For the present architecture and loading configuration, approximately five repeated unit cells in the lateral direction were required for the simulated effective elastic modulus to approach the homogenized prediction. The observed convergence at approximately five repeating unit cells applies to the present architecture, loading condition, and direction of repetition and should not be interpreted as a universal minimum unit cell number. This requirement should be considered when scaling the architecture to anatomically constrained applications. If the available anatomical dimensions permit fewer repeating units, boundary effects may become more influential, and the mechanical response should therefore be evaluated using direct full-scale simulations rather than assuming bulk homogenized properties.

Whereas homogenization informed the identification of candidate scaffold designs (Section 2.4), the FE simulations provided critical validation under conditions emulating mechanical testing. Notably, both selected designs (*i.e.*, Design A and B) preserved their intended zone-specific mechanical gradients in full-scale simulations, without introducing unintended stress peaks or discontinuities at the interfaces. Furthermore, the convergence study established a practical guideline for fabrication and testing. These further simulations strengthen the validity of the tri-zonal design approach and support the translation of computational design criteria into structurally and mechanically robust constructs suitable for experimental characterization and eventual biological evaluation.

2.7. Scaffold fabrication and morphological characterization

The 3D-printed Design A scaffolds closely replicated the intended tri-zonal architecture (Fig. 3a). The distinct regions, tendon-like, transitional, and bone-like, were clearly visible, and the strut arrangements were consistent with the original computer-aided design (CAD) model. No occluded pores or discontinuities were observed, and pore interconnectivity was preserved across all zones, a critical requirement for biological infiltration and fluid transport.

In contrast, Design B exhibited more frequent strut discontinuities, particularly in the tendon-like region, indicating that the lower density used approached the fabrication limits of the FDM process. This partial strut formation likely impacted both mechanical continuity and hydrogel infiltration.

In the scaffold design, pores in the tendon zone were expected to be stretched in one direction due to the strut-based geometry, whereas the gyroid TPMS geometry of the bone zone was expected to yield a network of smoothly curved pores. Pore dimensions in the printed scaffolds were quantified from 2D μCT cross-sections by fitting ellipses to individual pore openings. The corresponding major and minor axes were 1.03 ± 0.63 mm and 0.99 ± 0.60 mm in the tendon-like region, 0.71 ± 0.29 mm and 0.58 ± 0.18 mm in the transitional region, and 1.30 ± 0.10 mm and 0.60 ± 0.05 mm in the bone-like region. These measurements characterize the dimensions and shape of pore openings in the analyzed 2D sections and are not directly comparable with the 3D Euclidean-distance-based pore-size metric used in the computational design study.

The *SVF* values of 0.48 (bone), 0.53 (transition), and 0.14 (tendon), remained within acceptable deviations from the homogenized predictions (0.49, 0.45, and 0.19, respectively), confirming that the FDM process successfully produced zone-specific pore morphology.

Structural connectivity analysis on the binarized scaffold volume

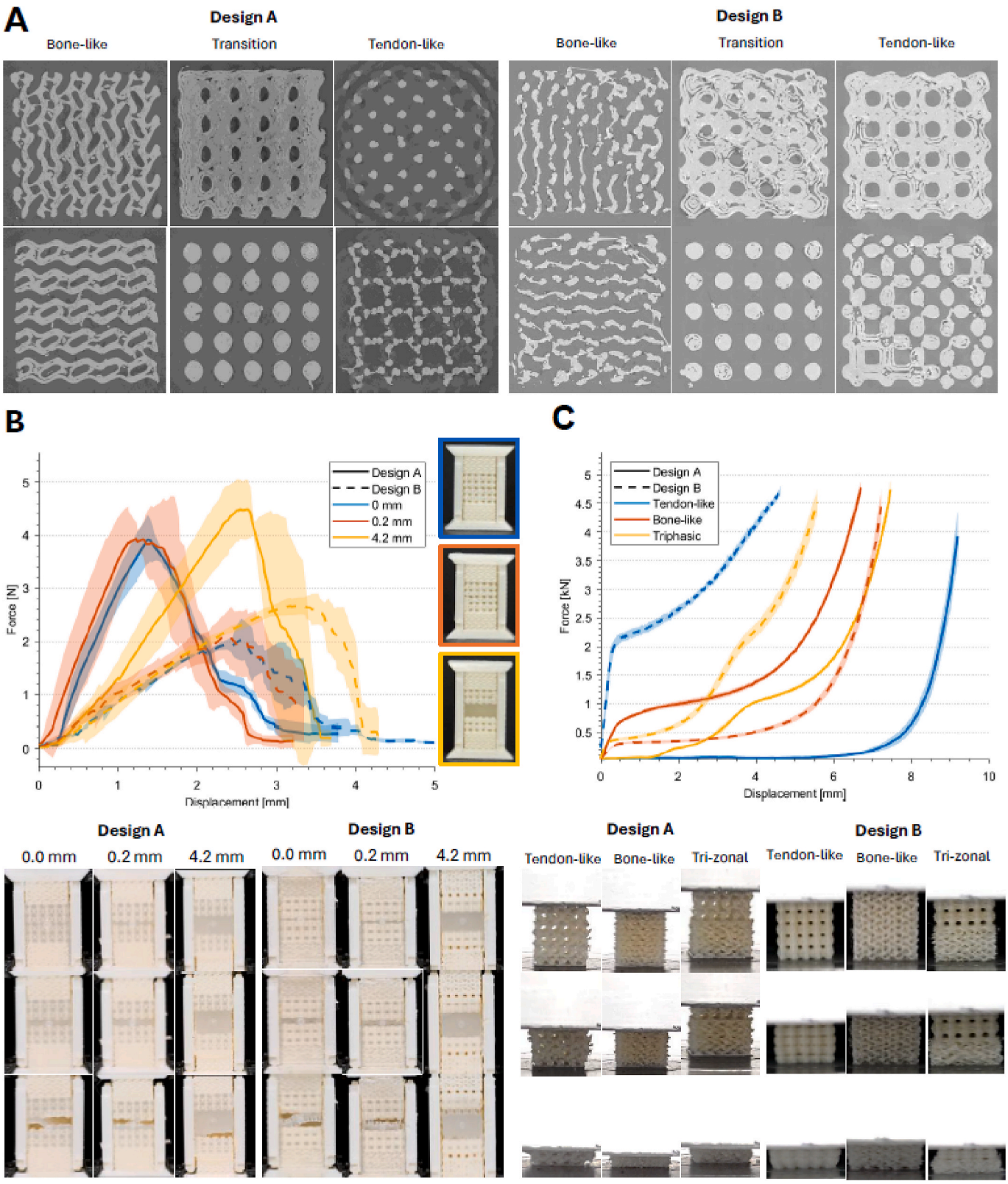


Fig. 3. Mechanical performance and structural fidelity of tri-zonal scaffolds. **a.** μCT reconstructions of 3D-printed tri-zonal scaffolds (Design A and B), visualizing internal architecture and zonal transitions between the bone-like, transition, and tendon-like regions. **b.** Tensile force–displacement curves for hydrogel-infused scaffolds of Design A (solid lines) and Design B (dashed lines) with different bulk hydrogel thicknesses (0.0 mm, 0.2 mm, and 4.2 mm, depicted in blue, orange, and yellow, respectively). Representative video frames illustrate the progression of failure during tensile loading. **c.** Compressive force–displacement curves for tri-zonal (yellow), fully bone-like (orange), and fully tendon-like (blue) scaffolds for both Design A (solid lines) and Design B (dashed lines). Inset images show deformation patterns under increasing compressive displacement. Data is presented as mean ± SD (n = 3). (For interpretation of the references to colour in this figure legend, the reader is referred to the web version of this article.)

($10 \times 10 \times 10$ mm^3) confirmed that Design B scaffolds were substantially less interconnected than Design A. The connectivity density (Conn. D) of Design A was 6274 mm^{-3}, compared to 21.262 mm^{-3} for Design B, representing a >290-fold reduction in interconnections per unit volume. This quantitative finding is consistent with visual observations of more disconnected struts in Design B. These fabrication differences should be considered when interpreting subsequent mechanical comparisons between Designs A and B, because the experimental performance reflects not only differences in the selected design parameters, but also their resulting manufacturability and structural fidelity.

These results validate the feasibility of using FDM to fabricate complex tri-zonal scaffolds with distinguishable mechanical regions, highlighting the printability limitations when pushing toward lower-density geometries.

2.8. Experimental validation of mechanical performance

The tensile tests evaluated the mechanical response of hydrogel-integrated constructs consisting of two tri-zonal scaffolds connected by an AlgGel hydrogel phase. Accordingly, the measured maximum tensile force represents a construct-level outcome rather than the intrinsic tensile strength of an individual scaffold. Design A exhibited higher maximum tensile forces than Design B across all tested hydrogel thicknesses (Fig. 3b). Maximum tensile forces ranged from 3.92 ± 0.46 N to 4.59 ± 0.56 N for Design A and from 2.03 ± 0.39 N to 2.67 ± 0.16 N for Design B, corresponding to approximately 72–93% higher values for Design A. These differences should be interpreted in the context of the complete construct, because the tensile response is influenced by scaffold architecture and print fidelity as well as hydrogel thickness, infiltration, and scaffold-hydrogel integration.

Interestingly, increasing the hydrogel thickness to 4.2 mm slightly improved the maximum tensile force for both designs, though differences were not statistically significant ($p > 0.05$) (Fig. 3b). This may be due to increased volume for stress distribution, though further investigation is needed.

The apparent tensile modulus, however, varied more substantially (Fig. 3b). In Design A, the apparent tensile modulus decreased significantly in the 4.2 mm group compared to 0.0 and 0.2 mm groups (0.65 ± 0.033 *vs* 1.00 ± 0.22 and 1.08 ± 0.21 MPa, respectively, $p < 0.01$), suggesting a transition to more hydrogel-dominated deformation. In contrast, Design B showed no significant difference in apparent tensile modulus across hydrogel thicknesses ($p > 0.05$), likely due to poor internal hydrogel infiltration possibly caused by the smaller pore sizes relative to Design A (Fig. 3a), limiting the extent of scaffold-gel mechanical integration. Differences between the numerically predicted and experimentally measured elastic response likely arise from the idealized assumptions of the computational models and fabrication-related effects in the printed scaffolds, including finite print resolution, local geometric deviations, strut coalescence, layer-wise manufacturing effects, and manufacturing defects. In addition, the constituent PLA properties used in the computational models were not calibrated using specimens printed under the exact processing conditions employed here. These factors may contribute to the remaining differences between the predicted and measured mechanical response. These results indicate that the construct-level tensile response reflects the combined effects of scaffold architecture, manufacturing fidelity, hydrogel thickness, and hydrogel integration.

Compression tests further demonstrated the functional influence of scaffold architecture. Both tri-zonal designs exhibited multi-zone stiffness curves, reflecting successive compression of individual zones (Fig. 3c).

In Design A, the tendon-like region ($\rho_t = 0.2$) showed compressive behavior comparable to the bone-like region of Design B ($\rho_b = 0.3$), highlighting the influence of local density over scaffold function. Conversely, the bone region of Design A remained significantly stiffer than any zone in Design B, confirming the enhanced load-bearing capacity enabled by higher density and surface-based TPMS geometry.

Despite differences in zone behavior, both designs displayed composite-like compression curves, characterized by stiffness plateaus and transitions, indicating stress redistribution between zones (Fig. 3c). This behavior supports the intended design function, which emulates the gradient mechanics of the native tendon-bone enthesis.

2.9. Fracture patterns of the hydrogel-integrated constructs

Visual analysis of the recorded tensile tests revealed different failure patterns between Designs A and B (Fig. 3b, bottom). In Design A, the first visible failure generally occurred within the hydrogel adjacent to the scaffold-hydrogel interface rather than within the PLA scaffold. In the 4.2-mm hydrogel group, pronounced hydrogel extension was observed before crack initiation, consistent with the lower apparent tensile modulus of these constructs. Following initiation, the crack propagated laterally through the hydrogel layer, in some cases leaving a thin hydrogel membrane temporarily connecting the scaffold ends (Fig. 3b). No fracture of the PLA scaffold was observed during these tests.

In Design B, failure was frequently observed around the outer hydrogel region. Post-test visual inspection showed incomplete hydrogel infiltration around portions of the scaffold, which may have contributed to the observed failure pattern (Fig. 3b). Because failure modes were not prospectively defined and dedicated fracture-surface characterization was not performed, these observations are interpreted qualitatively and do not establish a specific cohesive or interfacial fracture mechanism.

These results demonstrate that porosity and internal connectivity are essential for the integration of hydrogels and scaffolds, and that successful mechanical gradation depends not only on material selection but also on achieving sufficient interfacial continuity between phases.

The experimental results were broadly consistent with the differences predicted between the selected scaffold configurations, while also highlighting the importance of manufacturability and hydrogel integration. Design A combined favorable mechanical and morphological characteristics with higher print fidelity and more effective hydrogel infiltration. In contrast, Design B exhibited strut discontinuities and reduced hydrogel penetration, which likely contributed to its lower tensile performance. Accordingly, the comparison between Designs A and B should be interpreted as a comparison between an optimized configuration and a deliberately suboptimal reference, rather than as an isolated experimental validation of the optimization procedure itself.

These results highlight that pushing designs toward extreme density values may improve one performance criterion (*e.g.*, stiffness or compressive strength), but often comes at the expense of other critical features, such as porosity, printability, or soft-phase integration. Thus, scaffold design for soft-hard tissue interfaces requires a balanced, multi-objective approach that prioritizes both mechanical functionality and biological compatibility.

2.10. In vitro cell response to the scaffolds

To complement mechanical and morphological validation, the biological performance of the tri-zonal scaffolds of Design A and B (Fig. 4a) was preliminarily assessed *in vitro*, with a focus on cellular distribution and organization across the soft-hard interface. Given the scaffold's intended application in tendon-bone regeneration, these tests aimed to evaluate how well the scaffold architecture supports cell attachment and survival in spatially heterogeneous designed environments. To assess this, we performed fluorescence microscopy of preosteoblasts that were cultured for 7 days on scaffold A and B before fixation and staining for actin and the nucleus. Widefield images revealed notable differences in cell morphology and spatial arrangement between bone, transition, and tendon regions of each scaffold design (Fig. 4b).

On Design A (Fig. 4b, top row), preosteoblasts in the tendon zone adopted an elongated shape, often aligning along the struts, and in some cases spanning across the pore corners (Fig. 4b, top right). In contrast,

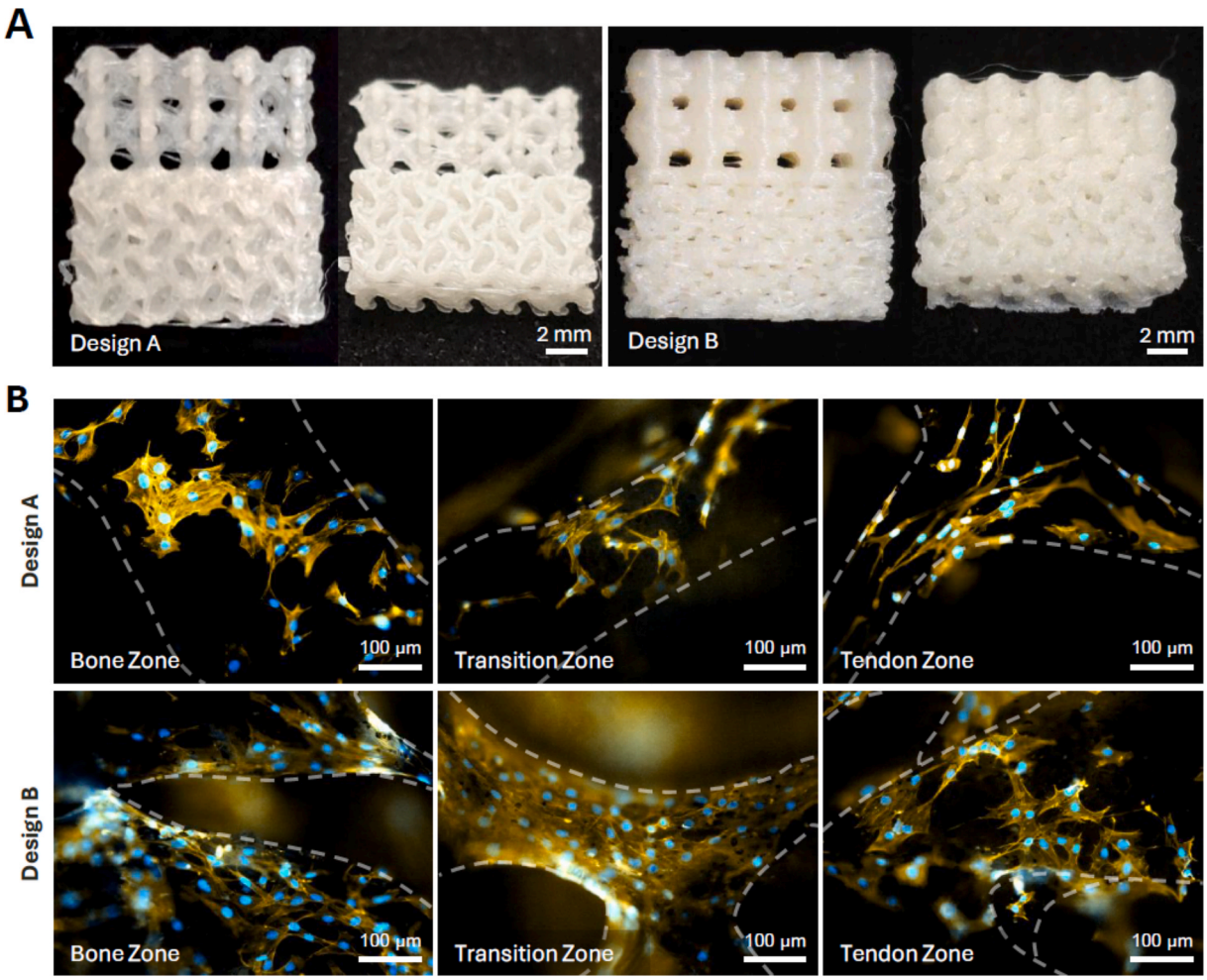


Fig. 4. *In vitro* response of MC3T3-E1 preosteoblasts to the tri-zonal scaffolds. **a.** Sample designs used for the cell experiments: Design A (left) and Design B (right). **b.** Fluorescence microscopy images of preosteoblasts after 7 days of culture on Design A and Design B (n = 6 scaffolds per design); images were acquired from the bone, transition, and tendon zones of each scaffold. Yellow represents the F-actin cytoskeleton (stained with rhodamine-phalloidin), and blue represents cell nuclei (stained with DAPI). Dashed lines outline the morphology of the underlying scaffold. (For interpretation of the references to colour in this figure legend, the reader is referred to the web version of this article.)

cells attached to the bone region exhibited a less polarized morphology, spreading more evenly in all directions. In addition, cells in the bone area of the scaffold tended to follow the curvature of the scaffold surfaces. In the transition zone, cells exhibited an intermediate shape, being more elongated than in the bone region but less so than in the tendon region.

For Design B (Fig. 4b, bottom row), the differences in cell shape between scaffold regions were less pronounced. Cells in the tendon region did not show a clear alignment along the struts, and they were able to spread in all directions, more than in the tendon area of Design A. By comparison, cells in the bone zone displayed less spreading than in Design A. We hypothesize that these effects could be related to local architectural differences between zones in Design B as compared to Design A. Specifically, the higher tendon-zone density ($\rho_t = 0.6$) results in smaller pores, but as shown by the morphological analysis in Section 2.2, it also leads to an increased scaffold surface area (A) due to the higher strut density. The larger available surface area may promote rapid early cell attachment and coverage, thereby reducing visible contact-guidance cues and enabling more isotropic spreading. Conversely, the bone zone in Design B is less dense than the tendon zone. It therefore exhibits larger pores, which may reduce continuous cell-substrate contact and contribute to the lower degree of spreading observed. The increased apparent cell number on Design B may also have influenced cellular organization through earlier confluence, which warrants further investigation.

These preliminary *in vitro* results provide essential biological context to the mechanically validated tri-zonal scaffold designs. Design A, which met all the mechanical and morphological targets, also displayed a more favorable effect of scaffold geometry on cell behavior than Design B. The observed differences in cell morphology and spatial organization between scaffold zones indicate that cells interact differently with the distinct local architectures. However, because the present study used only MC3T3-E1 preosteoblasts, these observations cannot be extrapolated to tenocyte- or fibrocartilage-specific responses or interpreted as evidence of lineage-specific differentiation. Scaffold-induced spatial instruction of alignment in the tendon zone, but not in the bone zone, is particularly relevant for tendon regeneration, as native tendon tissue relies on the parallel orientation of tenocytes and collagen fibers to achieve its high tensile strength [38,39]. These results underscore the necessity for a balanced, multi-objective optimization of the scaffolds, where the geometry, mechanics, structure stability, and induced cellular responses must be optimized to fulfil the biocompatibility requirements for regeneration of the bone-tendon interface.

2.11. General limitations and future recommendations

The threshold ranges used in the objective function were obtained from representative literature values and should therefore be regarded as guiding targets rather than universal constants. Native entheses

exhibit substantial inter-individual variability and site-specific differences (*e.g.*, rotator cuff vs. Achilles), including distinct loading modes and functional requirements. Accordingly, both the threshold values and their relative weights within the objective function should be treated as tunable inputs that can be re-parameterized for a specific anatomical site or for patient-specific target ranges when such data are available. Future implementations could further incorporate uncertainty-aware or robust optimization strategies to account for biological variability and manufacturing tolerances explicitly.

The computational analyses have several limitations. The FE model represented only the elastic PLA scaffold phase and did not include the hydrogel, scaffold-hydrogel interface, manufacturing defects, damage, or fracture. Its primary role was to complement the homogenization analysis by examining the elastic response of the assembled scaffold and the effect of finite unit cell repetition on the predicted effective stiffness. Consequently, the simulations should not be interpreted as predictions of failure or interfacial load transfer in the complete composite construct. In addition, the constituent PLA properties used in the computational models were not independently calibrated using specimens printed under the exact processing conditions employed for scaffold fabrication. Absolute stress and stiffness values should therefore be interpreted with caution, whereas the simulations are more appropriately used to compare relative elastic stress distributions and architectural responses. Future models should incorporate experimentally calibrated material and interface properties, manufacturing imperfections, and appropriate damage and fracture formulations.

The experimental comparison between Designs A and B does not fully isolate the contribution of the multi-objective design procedure from differences in manufacturability. Design B approached the printability limits of the FDM process and exhibited strut discontinuities and reduced hydrogel infiltration. Future studies should therefore include print-quality-matched comparator designs to more directly determine the experimental contribution of the design-selection strategy.

Similarly, the independent mechanical contribution of the Schwarz-P transitional region was not isolated because no biphasic/no-transition or topology-matched control was included. Our related work on hybrid strut-TPMS interfaces demonstrated that appropriately designed transition regions can reduce strain localization at the connection and shift failure into the adjoining substructures rather than the interface [40]. However, the present study does not establish that the Schwarz-P region independently provides the same function in the current PLA-hydrogel scaffold system. Future studies should include appropriate control architectures and quantitative local deformation measurements to determine the specific mechanical contribution of the transitional region.

The present study focused primarily on scaffold architecture, mechanical performance, manufacturing fidelity, and preliminary cell-scaffold interactions. Hydrogel rheology, swelling behavior, degradation kinetics, quantitative cellular infiltration, and scaffold-hydrogel interfacial adhesion were not comprehensively characterized. In addition, failure modes were assessed qualitatively rather than using prospectively defined classification criteria or dedicated fracture-surface analysis. Future studies should therefore combine physiochemical characterization of the hydrogel with synchronized mechanical testing, predefined failure classifications, and post-fracture imaging to distinguish cohesive hydrogel failure, scaffold-hydrogel interfacial failure, and scaffold fracture quantitatively.

The present study was also limited to quasi-static tensile and compressive mechanical characterization and therefore does not address cyclic damage accumulation, fatigue life, or stiffness degradation under repeated loading. Native entheses are predominantly subjected to cyclic and multiaxial loading *in vivo*, making fatigue behavior an important consideration for long-term performance. Future studies should combine cyclic simulations with experimental fatigue testing and could incorporate fatigue-relevant criteria, such as stiffness retention, damage accumulation, and fatigue life, into the multi-objective design framework.

Biological validation was limited to qualitative assessment of MC3T3-E1 cell attachment, morphology, and spatial organization. Quantitative measurements of viability, proliferation, morphology, orientation, phenotype, and extracellular-matrix production were not performed. Moreover, MC3T3-E1 preosteoblasts cannot represent tenocyte- or fibrocartilage-specific responses, the observed regional differences should not be interpreted as evidence of lineage-specific biological function. Further validation should therefore use enthesis-relevant cell types, including tenocytes, fibrocartilage-relevant cells, and multicellular or co-culture models, together with quantitative assessment of matrix deposition and phenotype-specific gene and protein expression. Relevant analyses could include alkaline phosphatase (ALP) activity, Alizarin Red staining, quantitative polymerase chain reaction (qPCR), Western blot analysis, and appropriate fibrosis- and vascularization-related markers.

Future research should also examine how hydrogel incorporation influences region-specific cellular responses. Improving hydrogel stability, for example through chemical crosslinking of the gelatin component or incorporation of adhesion-promoting peptides [41], may improve soft-phase integration and facilitate longer-term biological studies. Beyond providing a compliant phase, localization of the hydrogel to the tendon-like region could provide a modular compartment for region-specific biochemical functionalization. Tendon- or fibrocartilage-directed cues could be incorporated into the tendon-zone hydrogel, while distinct osteogenic cues could be presented on the bone-side scaffold. Such approaches may enable spatially defined biochemical instruction in addition to mechanical and topographical cues. The relative contributions of geometry, stiffness, and biochemical signaling should nevertheless be investigated independently to guide future scaffold optimization.

Recent gradient and TPMS scaffold studies have demonstrated that spatial variation in porosity, pore geometry, and lattice density can modify scaffold stiffness, deformation behavior, and biological transport properties [17,20,27]. However, quantitative comparison of absolute mechanical properties across studies is complicated by differences in material composition, manufacturing method, scaffold scale, and testing configuration. Design A differs principally in the assignment of distinct architectural families to the tendon-like, transitional, and bone-like regions and their simultaneous selection according to multiple mechanical and morphological criteria. A quantitative comparison with representative recent gradient, TPMS, and hybrid scaffold approaches is provided in Table S4 of the supplementary document. Absolute structural and mechanical values should not be directly ranked across studies because of the differences in materials, manufacturing processes, architectures, specimen geometries, and testing methods.

Overall, the present workflow provides a framework for integrating computational design, fabrication, mechanical characterization, and preliminary biological assessment of graded soft-hard tissue scaffolds. Further validation under physiologically relevant mechanical and biological conditions will be required to establish its translational applicability.

3. Conclusions

This study presents an integrated computational-experimental framework for designing, fabricating, and validating a tri-zonal scaffold-hydrogel system that emulates the mechanical and morphological complexity of the native bone-tendon enthesis. By utilizing homogenization-based parametric modeling and finite element simulations, we systematically explored the scaffold design space and identified hybrid architectures that can satisfy competing requirements for anisotropy, elastic modulus, Poisson's ratio, porosity, and interfacial gradients.

Two tri-zonal scaffold designs were fabricated via FDM 3D printing and, for mechanical tests, combined with an injected soft hydrogel phase (5% AlgGel), to enable both mechanical interlocking and biological

support. Mechanical testing confirmed that the optimized scaffold (Design A, with bone and tendon density ratios of 0.5 and 0.2) achieved superior tensile performance (72–93% higher than Design B) and stress transfer through a well-integrated gradient, while the suboptimal design (Design B, with respective densities of 0.3 and 0.6) revealed performance limitations due to poor hydrogel infiltration and reduced porosity. FE simulations showed intermediate elastic stress levels within the Schwarz-P transitional region. Although the use of such a transition was motivated by our previous work on mechanically robust hybrid strut-TPMS interfaces [40], its independent mechanical contribution was not isolated in the present study; therefore, no specific mechanical-buffer function is assigned to this region. Convergence analysis confirmed that a minimum of five unit cells is required to replicate homogenized material behavior at full scale.

In vitro studies using preosteoblast cells demonstrated that the scaffolds support cell adhesion and can guide their spatial distribution. In Design A, cells aligned along struts in the tendon region and adopted a relatively more spread shape in the bone region, whereas Design B showed less pronounced or reversed differences. These findings highlight the role of geometry and pore architecture in guiding region-specific cell organization, emphasizing their importance for designing cell-instructive soft–hard interface scaffolds.

Our results highlight the importance of a multi-objective scaffold design strategy that integrates mechanical, morphological and biological design requirements for the tendon-bone interface. The approach outlined here provides a robust platform for engineering, fabrication and *in vitro* testing of graded scaffolds for tendon-bone repair and other soft-hard tissue interfaces.

Future work should focus on stabilizing the hydrogel component to improve bioactivity, incorporating tissue-specific cues to promote zonal regeneration, and validating performance under dynamic and long-term culture conditions. This framework offers a promising direction toward the development of functional, clinically translatable scaffolds for regenerative medicine, particularly for tissue interface engineering.

4. Materials and methods

4.1. Bioinspired scaffold design and parametric modeling

Tri-zonal scaffold architectures were designed to replicate the mechanical and morphological gradients of the native tendon-bone enthesis. Scaffold geometries were generated as 3D voxel models using MATLAB (R2024a, MathWorks, USA), based on a previously published parametric design script by Yang et al. [42], which was adapted to allow precise control over input variables including tendon-zone density (ρ_t), bone-zone density (ρ_b), and the number of repeating unit cells along and across the scaffold. To ensure manufacturability by FDM and to prevent print-induced defects (*e.g.*, strut discontinuity and pore occlusion), the design space was constrained such that minimum strut thicknesses and minimum feature dimensions remained above the effective print resolution of the selected nozzle diameter and layer height.

The scaffold was divided into three functionally distinct regions: (*i*) a tendon-like zone composed of a compliant, strut-based face-centered cubic (FCC) lattice (including only the face-centered sites, while excluding cube-corner vertices) to replicate the deformable nature and anisotropy of soft connective tissue, (*ii*) a bone-like zone based on a dense, surface-based TPMS gyroid structure, selected for its high stiffness and morphological similarity to trabecular bone, and (*iii*) a transitional zone formed using a surface-based TPMS Schwarz primitive surface that blends properties of both regions to provide a smooth mechanical gradient across the interface.

Each geometry was voxelized and exported in both STL format for 3D printing and as Abaqus input files (.inp) for finite element modeling. This parametric approach enabled the design of scalable scaffolds tailored to both mechanical and biological testing requirements.

For mechanical testing, the scaffold was designed to consist of five unit cells ($2 \times 2 \times 2$ mm^3 each) along each axis, yielding total dimensions of $10 \times 10 \times 10$ mm^3. Each scaffold contained two units of tendon-like and bone-like regions at either end and a single transitional unit in the center. For biological assays, a thinner configuration ($2 \times 10 \times 10$ mm^3) was used to facilitate light penetration during microscopy, consisting of five parallel unit cells along one axis only.

This design strategy enabled the simultaneous control of key scaffold properties, including stiffness gradients, pore architecture, and anisotropy, thereby satisfying the conflicting mechanical and biological requirements inherent to soft-hard tissue interfaces.

4.2. Predictive computational modeling of scaffold mechanics

4.2.1. Parametric design optimization via homogenization

To guide scaffold design and identify configurations capable of replicating the mechanical and morphological features of the tendon-bone interface, a homogenization-based parametric study was performed in MATLAB (R2024a). The model estimated effective mechanical properties for a range of tri-zonal scaffold configurations by systematically varying the two key input parameters: bone-zone density (ρ_b) and tendon-zone density (ρ_t).

For each combination of ρ_b and ρ_t, a scaffold configuration was generated and subjected to numerical homogenization using periodic boundary conditions in all directions, following an established framework [43]. From each unit cell, the following parameters were computed: 1. stiffness matrix **C** using a three-dimensional numerical homogenization approach implemented in the MATLAB script *homo3D* (MathWorks, Natick, MA, USA) [43], 2. compliance matrix **S** as the inverse of **C** according to the generalized Hooke's law for anisotropic materials (Eq. (1)), 3. Zener ratio (z), as a measure of anisotropy (Eq. (2)), where $z = 1$ indicates isotropy and deviations from unity indicate anisotropy, 4. effective elastic modulus (E) in three directions (Eq. (3)), 5. Poisson's ratio (ν) in three planes (Eq. (4)), 6. solid volume fraction (*SVF*), calculated as the percentage of solid voxels relative to the total voxels (Eq. (5));, 7. pore size, determined using the Euclidean distance transform computed on the binary pore mask (26-connectivity) to measure the distance from each pore voxel to the nearest solid voxel, implemented using the *bwdist* function in MATLAB, and 8. surface area, as an indicator of cell-adhesive surface availability, determined from the 3D binary pore mask using a voxel-based surface reconstruction *via* the *regionprops3* function in MATLAB, which estimates object surface area by fitting triangulated surface meshes to the voxel boundaries.

$$\varepsilon = \mathbf{S} \bullet \boldsymbol{\sigma}, \quad \mathbf{S} = \mathbf{C}^{-1} \tag{1}$$

$$z = \frac{2C_{44}}{C_{11} - C_{12}} \tag{2}$$

$$E_i = \frac{1}{S_{ii}}, \quad i \in \{x, y, z\} \tag{3}$$

$$\nu_{ij} = -\frac{S_{ji}}{S_{ii}}, \quad i \neq j, i, j \in \{x, y, z\} \tag{4}$$

$$SVF = \frac{N_{solid}}{N_{solid} + N_{pore}} \times 100 \tag{5}$$

To ensure biomimetic relevance, six design constraints were imposed based on literature values for native tendon and bone tissue: Zener ratio: $z_b \approx 1$ (bone, isotropic) [31], $|z_t - 1| \gg 0$ (tendon, anisotropic) [9,32], elastic modulus ratio: $E_b : E_t > 9$ [3,4], Poisson's ratio: $\nu_b = 0.3$–0.35 (bone) [29], $-1.44 < \nu_t < -0.39$ (tendon, auxetic) [30], pore size: 200–400 μm for bone [25,26], 400–700 μm for tendon [23], *SVF*: 0.26–0.75 for bone [33], surface area-to-volume ratio: >30 cm^{-1} [34]. The specific target ranges and supporting references are also summarized in Table 1. Architectural continuity across the scaffold zones was considered separately through the use of the continuous Schwarz-P

Table 1
Literature-derived design criteria, target ranges, intended roles, and supporting references used in the multi-objective scaffold design framework.

Criterion	Target used	Intended role	References
Bone:tendon elastic modulus ratio	> 9	Represent soft-to-hard stiffness contrast	[3,4]
Tendon Poisson's ratio	−1.44 to −0.39	Tendon-like auxetic response	[30]
Bone Poisson's ratio	0.30–0.35	Bone-like conventional response	[29]
Zener ratio	Tendon: anisotropic; bone: near-isotropic	Zone-specific anisotropy	[31 9,32]
Tendon pore size	400–700 μm	Tendon-zone morphological target	[23]
Bone pore size	200–400 μm	Bone-zone morphological target	[25,26]
Bone solid volume fraction	0.26–0.75	Balance porosity and load-bearing material	[33]
Surface-area-to-volume ratio	>30 cm^{-1}	Increase available scaffold surface area	[34]

transitional geometry. The use of an intermediate transition architecture was motivated by our previous work showing that hybrid connections between strut-based and TPMS lattices can reduce strain localization at the connection and shift failure toward the adjoining constituent regions rather than the interface [40]. These literature-derived thresholds were used as design targets for the present proof-of-concept framework and should not be interpreted as universal values for all anatomical entheses.

To systematically evaluate these constraints, we implemented a composite objective function (Eq. (6)) that scores each parameter combination using 11 normalized penalty terms corresponding to the six quantitative design criteria. Each penalty term was assigned equal weight. A penalty of zero was assigned when the corresponding parameter fell within its target range, whereas increasing values reflected increasing deviation from the accepted range. The total objective-function value was obtained by summing the individual penalty terms, such that lower values indicated better overall agreement with the predefined design targets. Designs that satisfied all six quantitative criteria were selected as the optimal configuration (Design A), while those meeting the fewest but remaining printable were selected as the suboptimal comparison configuration (Design B), providing a lower-bound reference. These two configurations were selected for fabrication, experimental testing, and comparative evaluation.

$$
\begin{aligned}
OF(\rho_b,\rho_t) = &\left(\frac{\max(0,\ 9-\frac{E_b}{E_t})}{9}\right)^2 + \left(\frac{max(0,\ -1.44-\nu_t,\ \nu_t+0.39)}{1.05}\right)^2 \\
&+ \left(\frac{max(0,\ 0.30-\nu_b,\ \nu_b-0.35)}{0.05}\right)^2 \\
&+ \left(\frac{\max(0,\min(z_t,\ 2-z_t))}{1}\right)^2 + \left(\frac{|z_b-1|}{\max_i(|z_b^{(i)}-1|)}\right)^2 \\
&+ \left(\frac{max(0,\ 400-p_t,\ p_t-700)}{300}\right)^2 \\
&+ \left(\frac{max(0,200-p_b,p_b-400)}{200}\right)^2 \\
&+ \left(\frac{max(0,\ 0.26-SVF_b,\ SVF_b-0.75)}{0.49}\right)^2 \\
&+ \left(\frac{\max(0,\ 3-\frac{SA}{V})}{3}\right)^2
\end{aligned}
\tag{6}
$$

$term_E$ = penalizes insufficient bone-to-tendon modulus ratio.
$term_{\nu,t}$, $term_{\nu,b}$ = penalize tendon- and bone-zone Poisson's ratios outside their target ranges.
$term_{Z,t}$, $term_{Z,b}$ = penalize insufficient tendon anisotropy and deviation from bone isotropy.
$term_{p,t}$, $term_{p,b}$ = penalize tendon- and bone-zone pore sizes outside the literature-derived ranges.
$term_{SVF}$ = penalizes bone-zone solid volume fraction outside its target range.
$term_{SA/V}$ = penalize insufficient surface-area-to-volume ratio in the bone, transition, and tendon zones.

The composite objective function consisted of 11 normalized penalty terms corresponding to the six quantitative design criteria. A penalty of zero was assigned when a parameter was within its predefined target range, whereas increasing values represented increasing deviations from that range. All 11 normalized penalty terms were assigned equal weight and summed to obtain the total objective-function value; no additional criterion-specific weighting factors were applied. Equal weighting was used to avoid introducing unsupported preferential weighting among the predefined criteria; the robustness of this assumption was subsequently evaluated through criterion-weight sensitivity analysis.

An a posteriori Pareto analysis was performed across the 36 feasible scaffold configurations using the 11 normalized penalty terms of the objective function as independent minimization objectives. A configuration was considered dominated when another feasible configuration exhibited an equal or lower penalty for all 11 objectives and a strictly lower penalty for at least one objective. Configurations for which no dominating alternative existed were classified as Pareto-optimal.

Criterion-weight sensitivity analysis was performed by independently varying the weight of each of the six quantitative design-criterion categories to 0.5× and 2× its baseline value, while maintaining the baseline weights for all remaining criteria. For criteria represented by multiple zone-specific penalty terms, the same weighting factor was applied to all corresponding terms. The resulting weighted objective-function values and design rankings were compared across all weighting scenarios.

4.2.2. *Finite-element simulation of tri-zonal scaffold behavior*

To validate the results of the homogenization study and to analyze stress distribution and deformation behavior under loading, full-scale finite element simulations were performed using Abaqus/CAE 2022 (v6.25, SIMULIA, Dassault Systèmes, France).

Each scaffold model incorporated the complete hard phase tri-zonal architecture of Design A, consisting of two tendon-like units, one transitional unit, and two bone-like units, in alignment with the experimental specimens. The voxel-based geometries were meshed using C3D8R (8-node linear brick, reduced integration) elements. To optimize the mesh for both accuracy and computational efficiency, selection of the number of voxels was informed by a voxel sensitivity analysis (Supplementary Note 1). This analysis led us to use 64×10^3 ($40 \times 40 \times 40$) voxels per unit cell, resulting in voxel edges of 0.05 mm. All scaffold regions were modeled as linearly elastic using a PLA elastic modulus of E = 3071 MPa, consistent with the value used in the homogenization analysis, and a Poisson's ratio of $\nu = 0.45$. The analyses were performed using a *static, general* step with geometric nonlinearity enabled (NLGEOM=ON).

The FE model represented only the PLA scaffold phase and was intended to characterize the elastic response of the scaffold architecture under the prescribed loading conditions. The model was also used to assess the effect of the number of repeated unit cells on the predicted effective stiffness and to compare the finite scaffold response with the homogenization-based predictions. This comparison was used to evaluate the influence of finite-size and boundary effects and the extent to which the periodic homogenization assumption was representative of

the assembled scaffold architecture. The hydrogel phase, scaffold-hydrogel interface, manufacturing defects, damage, and fracture were not included. Accordingly, the simulations were not used to predict failure or fracture behavior of the experimentally tested composite constructs.

For tensile simulations, a vertical displacement of 0.1 units (1% strain) was applied to the top surface, while the bottom surface was fixed in the loading direction (z-axis). Compression simulations used the same constraints with the applied displacement direction inverted. In both loading cases, lateral surfaces were left unconstrained to allow natural Poisson-driven deformation.

Engineering stress at each increment was calculated as the reaction force at the loaded surface divided by the initial cross-sectional area, $\sigma = F_z/A_0$, and engineering strain as the applied displacement divided by the initial scaffold height, $\varepsilon = \Delta u_z/H_0$. The elastic modulus was obtained from the two-point slope between the first and final increments of the loading step (Eq. (7)).

$$E_{FE} = \frac{\sigma_{final} - \sigma_{initial}}{\varepsilon_{final} - \varepsilon_{initial}} \tag{7}$$

From the FE simulations, we extracted global scaffold stiffness, stress–strain distribution maps, deformation fields, and stress concentration zones. These simulation outputs were compared against homogenization predictions to verify model convergence and mechanical gradient fidelity. These analyses were used to compare zone-specific elastic stress distributions, deformation patterns, and global scaffold stiffness between the selected architectures.

4.3. Mechanical characterization of fabricated tri-zonal scaffolds

4.3.1. Scaffold fabrication via FDM

Scaffold designs selected from the computational study (Design A and Design B) were fabricated using an FDM printer (Ultimaker 2+, Ultimaker B.V., Netherlands) equipped with a 0.25 mm nozzle. PLA filament was used as the printing material, selected for its biocompatibility and mechanical stability. All the scaffolds were 3D printed with a layer thickness of 0.1 mm, a print speed of 30 mm/s, and a nozzle temperature of 210 °C. The print bed was maintained at 60 °C, with a cooling fan speed of 100%. A 100% infill density was applied to ensure consistent internal geometry and structural performance. Each scaffold was printed in the upright orientation, corresponding to the loading axis in subsequent mechanical testing, to preserve the alignment of the tri-zonal architecture. No support material was required to create the lattice. Strut discontinuity was minimized by printing with a combination of a small nozzle diameter, thin layers, and an upright build orientation, which reduces unsupported span length and promotes continuous layer-to-layer fusion along strut axes. Aperture occlusion was mitigated by calibrating extrusion for thin features and by using high cooling (100% fan) in combination with a moderate print speed (30 mm/s) to limit filament sagging and over-deposition at pore edges, which are common causes of partial pore closure in open structures.

Print fidelity, particularly in the low-density tendon region, was verified by visual inspection of pore openness and strut continuity before testing, as well as by μCT-based assessment of the printed internal architecture (Fig. 3a), which was used to confirm accurate restoration of the designed pore network and zonal transitions.

4.3.2. Hydrogel formulation and crosslinking

The soft connective phase was created using a hybrid hydrogel formulation (5% AlgGel) consisting of 5% (w/v) sodium alginate (Fisher Scientific, Belgium) and 5% (w/v) gelatin Type A (Merck Sigma-Aldrich, Germany) dissolved in 0.9% NaCl solution. The solution was stirred at 40 °C until fully dissolved to prevent premature gelation of gelatin. After injection into the mold, ionic crosslinking of the alginate component was achieved by immersion in 200 mM $CaCl_2$ for 12 h at room temperature. This formulation was chosen to combine the structural integrity of ionically crosslinked alginate with the bioadhesive properties of gelatin, promoting both mechanical and biological integration.

4.3.3. Compression testing of mono- and tri-zonal scaffolds

Compression tests were performed using a mechanical testing machine (LR-5 K, Lloyd Instruments Ltd., UK) equipped with a 5 kN load cell. Specimens were compressed between two flat steel plates at a constant displacement rate of 0.05 mm/s until a deformation of 9 mm was achieved. Three scaffold types were tested in triplicate ($n = 3$): full tri-zonal scaffolds, tendon-only scaffolds, and bone-only scaffolds. To enable direct comparison, the mono-zonal scaffolds were designed with five repeating units along the loading direction (a total height of 10 mm), matching the dimensions of the tri-zonal specimens, and used the same densities (ρ_b, ρ_t) as the corresponding bone-like and tendon-like zones in the tri-zonal scaffolds. Compression tests were corrected for machine compliance, determined from a reference test in which the compression plates were brought into direct contact without a specimen [44]. The resulting force–displacement curve was fitted in MATLAB with a two-term exponential function, and the fitted compliance was subtracted from all experimental force–displacement data to isolate the true deformation behavior of the scaffold.

4.3.4. Tensile testing of hydrogel-integrated scaffold constructs

To evaluate the tensile performance and interfacial behavior of the tri-zonal scaffold in combination with a compliant hydrogel phase, custom molds were designed to embed the 5% (w/v) alginate-5% (w/v) gelatin (AlgGel) hydrogel between two scaffold specimens. Scaffolds were positioned with their tendon-like regions facing inward, thereby creating a central hydrogel bridge that represents a soft biological interface (Fig. 1d). The hydrogel layer thickness was controlled by the fixed spacing between the two scaffold specimens, defined by the mold geometry, using three molds with inter-scaffold spacings of 0, 0.2, and 4.2 mm. After gelation, the hydrogel thickness corresponded to the mold-defined spacing and was verified by direct measurements of the final construct using digital calipers before mechanical testing. The mold ensured precise alignment and enabled infiltration of the hydrogel into the porous scaffold. Lateral slits facilitated uniform diffusion of the crosslinking agent. After ionic crosslinking, the construct consisted of two rigid PLA scaffolds mechanically interlocked with the central hydrogel phase. Following crosslinking, specimens were kept immersed in the $CaCl_2$ solution until mechanical testing. Each construct was removed immediately before testing and mounted on the tensile tester without an additional drying step, thereby minimizing changes in hydrogel hydration prior to loading.

Tensile tests were performed using the same testing system equipped with a 50 N load cell. Custom 3D-printed PLA grips interfaced with printed side tabs located below each scaffold's bone region, allowing secure mounting without applying preload. Constructs were subjected to uniaxial tensile loading at 0.05 mm/s until failure, defined as complete separation at the hydrogel interface. Force and displacement data were recorded for three replicates per group ($n = 3$).

4.3.5. Mechanical data processing and analysis

The maximum tensile force was defined as the highest measured force before failure and is reported as a construct-level mechanical outcome without area normalization. Stiffness, k, was determined from the slope of the force–displacement curve. The apparent tensile modulus was calculated as $E_{app} = k \cdot L_0/A_0$, where L_0 is the initial gauge length defined as the distance between the outer edges of the bone-like regions of the two opposing scaffolds, and A_0 is the nominal external cross-sectional area perpendicular to the loading direction. Because the construct is porous and contains both PLA and hydrogel phases, E_{app} is reported as an apparent construct-level modulus rather than an intrinsic material property. All values are reported as mean ± standard deviation

($n = 3$ per group).

4.3.6. Micro-computed tomography and pore characterization

μCT imaging was used to assess the geometric fidelity and pore architecture of the 3D-printed scaffolds. Specimens were scanned using a ZEISS Xradia Context scanner (Carl Zeiss AG, Germany) with a source current of 66 μA, a voltage of 60 kV, and an exposure time of 1.5 s per projection. The scans were acquired with 966 projections, with an isotropic voxel size of 11.3 μm. Projection images were reconstructed into cross-sectional slices using the scanner's proprietary reconstruction software (Reconstructor Scout-and-Scan Control System, v.16.2.18058, Carl Zeiss AG, Germany). Reconstructed slices were imported into ImageJ for ROI selection, thresholding, and quantitative analysis using the BoneJ plugin [45]. No image filtering or smoothing was applied. The ROI encompassed the complete reconstructed scaffold volume ($10 \times 10 \times 10$ mm^3). Images were segmented using Otsu thresholding [46]. Individual pore openings in the binarized cross-sections were fitted with ellipses, and the corresponding major and minor axes were recorded as 2D pore-opening dimensions. These measurements are distinct from the 3D Euclidean-distance-based pore-size metric used in the computational analysis. A total of 2 independently printed scaffolds per design and 8 pore openings per zone per scaffold were analyzed. Values are reported as mean ± standard deviation. These measurements were used to characterize the pore geometry and structural fidelity of the printed scaffolds.

4.4. Cell-scaffold interactions

4.4.1. Scaffold sterilization

Scaffold sterilization was performed by immersion in 70% ethanol, followed by 20 min of UV exposure in a sterile laminar flow hood. All media and aqueous solutions used for cell culture were sterilized using a 0.2 μm syringe filter.

4.4.2. Cell preculture and seeding

Mouse preosteoblasts (MC3T3-E1, Sigma Aldrich, Germany) were used to evaluate the cytocompatibility of the tri-zonal scaffolds. Therefore, the cells were precultured for 2 days at 37 °C and 5% CO_2 in α-minimum essential medium (α-MEM without nucleosides), supplemented with 10% (v/v) fetal bovine serum and 1% (v/v) penicillin–streptomycin (Thermo Fisher Scientific, USA). The culture medium was refreshed every two days.

Preosteoblasts (10^5 cells/100 μL) were seeded in droplets onto each scaffold ($10 \times 10 \times 2$ mm^3) placed in 24-well plates to maximize initial cell-scaffold contact and minimize cell loss into the surrounding well during the seeding process. The samples were incubated for 4 h to promote initial attachment, followed by addition of 400 μL cell culture medium, for a total of 500 μL medium per well. From day 2 onwards, osteogenic culture medium supplemented with 50 μg/mL ascorbic acid and 4 mM β-glycerophosphate (Sigma-Aldrich, Germany) was used. The samples were incubated up to 7 days and the medium was refreshed every 2–3 days.

All the assays were performed in triplicate, and each experiment was repeated twice to ensure reproducibility (n = 6).

4.4.3. Fluorescence staining for cell morphology

To visualize cell morphology, cytoskeleton and nucleus staining were performed. Specimens were washed in phosphate buffer saline (PBS) and fixed using 4% paraformaldehyde for 15 min at room temperature. After another PBS washing, permeabilization was performed using 0.5% Triton X-100 in PBS (5 min, 4 °C), followed by blocking in 1% BSA/PBS (5 min, 37 °C). Cytoskeleton staining was performed with rhodamine–phalloidin (1:1000 in 1% BSA/PBS, 1 h, 37 °C), followed by PBS-Tween washes. DAPI (1:1000 in PBS) was used for nuclear staining (3 min, dark).

4.4.4. Fluorescence microscopy

Fluorescence imaging was performed using an upright fluorescence microscope (Nikon Eclipse LV100D-U, Nikon Corporation, Japan) equipped with a monochrome camera and interchangeable fluorescence filter cubes. Images were acquired using a 20× objective (NA 0.50) with filter cubes corresponding to rhodamine–phalloidin (cytoskeleton) and DAPI (nuclei). Each channel was captured separately in grayscale and subsequently pseudocolored in ImageJ for clarity (yellow: cytoskeleton; blue: nuclei). Brightness and contrast for each fluorescence channel were adjusted independently to optimize the visualization of the cytoskeleton and nuclear signals. Adjustments varied between images depending on signal intensity.

4.5. Statistical analysis

All statistical analyses were conducted using IBM SPSS Statistics 29 (IBM Corp., USA) to evaluate differences between experimental groups. One-way analysis of variance (ANOVA) was performed to assess the effects of scaffold design and experimental setup on mechanical performance. Where applicable, *post hoc* pairwise comparisons were performed using the Bonferroni correction to identify specific group differences.

Assumptions of normality and homogeneity of variances were tested using the Shapiro-Wilk test [47] and Levene's test [48], respectively. Only datasets meeting both criteria were subjected to ANOVA to ensure statistical robustness. Results were considered statistically significant at $p < 0.05$. All data are reported as mean ± standard deviation, unless otherwise stated. As a descriptive measure of specimen-to-specimen variability, the coefficient of variation was calculated for each mechanical-test group as $CV = (SD/mean) \times 100\%$, with the resulting values reported in Supplementary Table S5.

CRediT authorship contribution statement

L.B. Kunkels: Writing – review & editing, Writing – original draft, Visualization, Validation, Methodology, Formal analysis, Data curation. **J. Yang:** Methodology. **M. Klimopoulou:** Resources. **E. Yarali:** Methodology. **J. Li:** Data curation. **M.A. Leeflang:** Resources. **R.P. Tas:** Resources. **L.E. Fratila-Apachitei:** Writing – review & editing, Supervision. **A.A. Zadpoor:** Writing – review & editing, Supervision, Funding acquisition. **M.J. Mirzaali:** Writing – review & editing, Supervision, Funding acquisition.

Funding

This project was part of the NWO grant OCENW.XS22.2.044 obtained by M.J.M.

Declaration of competing interest

The authors declare that they have no known competing financial interests or personal relationships that could have appeared to influence the work reported in this paper.

Appendix A. Supplementary material

Supplementary material to this article can be found online at https://doi.org/10.1016/j.matdes.2026.117305.

Data availability

Data will be made available on request.

References

[1] U.G.K. Wegst, et al., Bioinspired structural materials, Nat. Mater. 14 (1) (2015) 23–36.
[2] M.C. Saldivar, et al., Bioinspired rational design of bi-material 3D printed soft-hard interfaces, Nat. Commun. 14 (1) (2023) 7919.
[3] T. Matsuhashi, et al., Tensile properties of a morphologically split supraspinatus tendon, Clin. Anat. 27 (5) (2014) 702–706.
[4] K. Choi, et al., The elastic moduli of human subchondral, trabecular, and cortical bone tissue and the size-dependency of cortical bone modulus, J. Biomech. 23 (11) (1990) 1103–1113.
[5] M. Amaral, et al., Densification route and mechanical properties of Si3N4-bioglass biocomposites, Biomaterials 23 (3) (2002) 857–862.
[6] A. Tits, D. Ruffoni, Joining soft tissues to bone: Insights from modeling and simulations, Bone Rep. 14 (2021) 100742.
[7] C. Pitta Kruize, et al., Biomimetic approaches for the design and fabrication of bone-to-soft tissue interfaces, ACS Biomater Sci. Eng. (2021).
[8] L. Rossetti, et al., The microstructure and micromechanics of the tendon–bone insertion, Nat. Mater. 16 (6) (2017) 664–670.
[9] A. Tits, et al., Local anisotropy in mineralized fibrocartilage and subchondral bone beneath the tendon-bone interface, Sci. Rep. 11 (1) (2021).
[10] L.M. Cross, et al., Nanoengineered biomaterials for repair and regeneration of orthopedic tissue interfaces, Acta Biomater. 42 (2016) 2–17.
[11] R. Balokhonov, V. Romanova, On the problem of strain localization and fracture site prediction in materials with irregular geometry of interfaces, Facta Univ. Ser.: Mech. Eng. 17 (2) (2019) 169.
[12] J.H. Waite, et al., Exploring molecular and mechanical gradients in structural bioscaffolds, Biochemistry 43 (24) (2004) 7653–7662.
[13] S. Thomopoulos, V. Birman, G.M. Genin, Structural interfaces and attachments in biology. (2013).
[14] Z. Wu, Stress concentration analyses of bi-material bonded joints without in-plane stress singularities, Int. J. Mech. Sci. 50 (4) (2008) 641–648.
[15] Y. Gao, et al., Toughening of hydrogel adhering interface based on soft/hard heterogeneous structures, Extreme Mech. Lett. 61 (2023).
[16] C. Pitta Kruize, et al., Biomimetic approaches for the design and fabrication of bone-to-soft tissue interfaces, ACS Biomater Sci. Eng. 9 (7) (2023) 3810–3831.
[17] P. Shang, et al., Gradient bipolar nanofiber scaffolds with a structure of biomimetic tendon-bone interface as rotator cuff patches, ACS Appl. Polym. Mater. 5 (8) (2023) 6107–6116.
[18] C.J. Peniche Silva, et al., Enthesis healing is dependent on scaffold interphase morphology-results from a rodent patellar model, Cells 11 (11) (2022).
[19] G. Criscenti, et al., Triphasic scaffolds for the regeneration of the bone-ligament interface, Biofabrication 8 (1) (2016) 015009.
[20] L. Li, et al., Design of a Haversian system-like gradient porous scaffold based on triply periodic minimal surfaces for promoting bone regeneration, J. Adv. Res. 54 (2023) 89–104.
[21] W. Gong, et al., Trabecular-like scaffold dictates osteogenesis via fluid shear stress-induced metabolic reprogramming through the CAV1-HIF-1alpha axis, Research (Wash D C) 9 (2026) 1307.
[22] S. Zhang, et al., A review on the use of computational methods to characterize, design, and optimize tissue engineering scaffolds, with a potential in 3D printing fabrication, J. Biomed. Mater. Res. B Appl. Biomater. 107 (5) (2019) 1329–1351.
[23] D.C. Markel, et al., Attachment and growth of fibroblasts and tenocytes within a porous titanium scaffold: a bioreactor approach, Arthroplast. Today 14 (2022) 231–236 e1.
[24] Z.-Y. Qiu, Y. Cui, X.-M. Wang, Natural bone tissue and its biomimetic, in: Mineralized Collagen Bone Graft Substitutes, 2019, pp. 1–22.
[25] A. Schroeder, et al., Effect of scaffold pore size on cell behaviour in vitro, Biomedizinische Technik/Biomed. Eng. 41 (s1) (1996) 436–437.
[26] H. Luan, et al., The effect of pore size and porosity of Ti6Al4V scaffolds on MC3T3-E1 cells and tissue in rabbits, Sci. China Technol. Sci. 62 (7) (2019) 1160–1168.
[27] X. Zhang, et al., Revealing the apparent and local mechanical properties of heterogeneous lattice: a multi-scale study of functionally graded scaffold, Virtual Phys. Prototyp. 18 (1) (2022).
[28] K. Wang, et al., A review of protein adsorption on bioceramics, Interface Focus 2 (3) (2012) 259–277.
[29] F. Katsamanis, D.D. Raftopoulos, Determination of mechanical properties of human femoral cortical bone by the Hopkinson bar stress technique, J. Biomech. 23 (11) (1990) 1173–1184.
[30] R. Gatt, et al., Negative Poisson's ratios in tendons: an unexpected mechanical response, Acta Biomater. 24 (2015) 201–208.
[31] D.M. Geraldes, A.T. Phillips, A comparative study of orthotropic and isotropic bone adaptation in the femur, Int. J. Numer. Method Biomed. Eng. 30 (9) (2014) 873–889.
[32] H. Khayyeri, et al., Comparison of structural anisotropic soft tissue models for simulating Achilles tendon tensile behaviour, J. Mech. Behav. Biomed. Mater. 61 (2016) 431–443.
[33] E.F. Morgan, H.H. Bayraktar, T.M. Keaveny, Trabecular bone modulus-density relationships depend on anatomic site, J. Biomech. 36 (7) (2003) 897–904.
[34] C. Torres-Sanchez, et al., Comparison of selective laser melted commercially pure titanium sheet-based triply periodic minimal surfaces and trabecular-like strut-based scaffolds for tissue engineering, Adv. Eng. Mater. 24 (1) (2021).
[35] M.C. Saldívar, et al., Rational positioning of 3D-printed voxels to realize high-fidelity multifunctional soft-hard interfaces, Cell Rep. Phys. Sci. 4 (9) (2023).
[36] J. Apostolakos, et al., The enthesis: a review of the tendon-to-bone insertion, Muscles Ligaments Tendons J 4 (3) (2014) 333–342.
[37] A.G. Schwartz, et al., Mineral distributions at the developing tendon enthesis, PLoS One 7 (11) (2012) e48630.
[38] W. Liu, Y. Cao, Tissue-engineering technology for tissue repair and regeneration, in comprehensive, Biotechnology (2011) 353–375.
[39] J. Buschmann, G. Meier Bürgisser, Structure and function of tendon and ligament tissues, Biomech. Tendons Ligaments (2017) 3–29.
[40] J. Yang, V. Moosabeiki, L. Bai, M.C. Saldívar, M.A. Leeflang, X. Chen, A. A. Zadpoor, M.J. Mirzaali, Strategy for hybrid connection of porous strut and triply periodic minimal surface lattice structures, Nat. Commun. (2026), 9699.
[41] I. Sandvig, et al., RGD-peptide modified alginate by a chemoenzymatic strategy for tissue engineering applications, J. Biomed. Mater. Res. A 103 (3) (2015) 896–906.
[42] J. Yang, et al., Rational design and additive manufacturing of grain boundary-inspired, multi-architecture lattice structures, Mater. Des. 235 (2023).
[43] G. Dong, Y. Tang, Y.F. Zhao, A 149 line homogenization code for three-dimensional cellular materials written in matlab, J. Eng. Mater. Technol. 141 (1) (2019).
[44] S.R. Kalidindi, A. Abusafieh, E. El-Danaf, Accurate characterization of machine compliance for simple compression testing, Exp. Mech. 37 (2) (1997) 210–215.
[45] M. Doube, et al., BoneJ: free and extensible bone image analysis in ImageJ, Bone 47 (6) (2010) 1076–1079.
[46] N. Otsu, A threshold selection method from gray-level histograms, IEEE Trans. Syst. Man Cybern. 9 (1) (1979) 62–66.
[47] S.S. Shapiro, M.B. Wilk, An analysis of variance test for normality (complete samples), Biometrika 52 (3–4) (1965) 591–611.
[48] B. Mandelbrot, Contributions to probability and statistics: essays in honor of Harold Hotelling, in: I. Olkin, S.G. Ghurye, W. Hoeffding, W.G. Madow, H.B. Mann (Eds.), SIAM Review, vol. 3(1), 1961, p. 80.